

# **Energy Budget of Plasma Motions, Heating, and Electron Acceleration in a Three-loop Solar Flare**

Gregory D. Fleishman<sup>1,2</sup>, Lucia Kleint<sup>3,4</sup>, Galina G. Motorina<sup>5,6</sup>, Gelu M. Nita<sup>1</sup>, and Eduard P. Kontar<sup>7</sup>, Center For Solar-Terrestrial Research, New Jersey Institute of Technology, Newark, NJ 07102, USA

2 Ioffe Institute, Polytekhnicheskaya, 26, St. Petersburg, 194021, Russia

3 Leibniz-Institut für Sonnenphysik (KIS), Schöneckstrasse 6, D-79104 Freiburg, Germany

4 University of Geneva, CUI, 7 route de Drize, 1227 Carouge, Switzerland

5 Astronomical Institute of the Czech Academy of Sciences, 251 65 Ondřejov, Czech Republic

6 Central Astronomical Observatory at Pulkovo of Russian Academy of Sciences, St. Petersburg, 196140, Russia

7 School of Physics & Astronomy, University of Glasgow, Glasgow G12 8QQ, UK

Received 2020 August 10; revised 2021 March 30; accepted 2021 March 31; published 2021 May 28

#### **Abstract**

Nonpotential magnetic energy promptly released in solar flares is converted to other forms of energy. This may include nonthermal energy of flare-accelerated particles, thermal energy of heated flaring plasma, and kinetic energy of eruptions, jets, upflows/downflows, and stochastic (turbulent) plasma motions. The processes or parameters governing partitioning of the released energy between these components are an open question. How these components are distributed between distinct flaring loops and what controls these spatial distributions are also unclear. Here, based on multiwavelength data and 3D modeling, we quantify the energy partitioning and spatial distribution in the well-observed SOL2014-02-16T064620 solar flare of class C1.5. Nonthermal emission of this flare displayed a simple impulsive single-spike light curve lasting about 20 s. In contrast, the thermal emission demonstrated at least three distinct heating episodes, only one of which was associated with the nonthermal component. The flare was accompanied by upflows and downflows and substantial turbulent velocities. The results of our analysis suggest that (i) the flare occurs in a multiloop system that included at least three distinct flux tubes; (ii) the released magnetic energy is divided unevenly between the thermal and nonthermal components in these loops; (iii) only one of these three flaring loops contains an energetically important amount of nonthermal electrons, while two other loops remain thermal; (iv) the amounts of direct plasma heating and that due to nonthermal electron loss are comparable; and (v) the kinetic energy in the flare footpoints constitutes only a minor fraction compared with the thermal and nonthermal energies.

*Unified Astronomy Thesaurus concepts:* Solar flares (1496); Solar x-ray emission (1536); Solar radio emission (1522); Solar extreme ultraviolet emission (1493); Solar magnetic fields (1503); Solar coronal heating (1989)

Supporting material: animations

# 1. Introduction

Solar flares are explosive phenomena that cover a range of heights in the solar atmosphere. Flares are observed as transient brightenings throughout the electromagnetic spectrum. Some of the brightenings can show apparent motions, while others can appear immobile. Solar flares can be associated with large-scale coronal mass ejections (CMEs), collimated jets, and/or solar energetic particles (SEPs) detected at the heliosphere. All these observables are associated with underlying magnetic, nonthermal, thermal, kinetic, and potential energies, whose transformation chains, partitions, spatial distributions, and temporal evolution are of primary importance for understanding the solar flare phenomenon.

Emslie et al. (2012) analyzed the energetics of 38 eruptive solar flares and, in particular, concluded that (i) the energy of flare-accelerated charged particles exceeds the bolometric energy radiated across all wavelengths and, thus, sufficient to supply this radiation; (ii) the electrons and ions accelerated in the flare gain comparable amounts of energy; and (iii) the free magnetic energy available in the given active region is sufficient to drive the particle acceleration and plasma heating and power the CME. Although these are important findings that confirm our overall understanding of the solar flare energy budget, the flare energy estimates (i) have large uncertainties, (ii) likely contain bias related to selection of a set of rather

strong flares, (iii) do not provide unambiguous temporal relationships between various components, and (iv) do not include the kinetic energy of turbulence or bulk motions of the thermal plasma in the flaring loops. Although the turbulent energy can be evaluated using the spectral broadening of relevant spectral lines (e.g., Kontar et al. 2017; Warren et al. 2018, and references therein), removing or at least minimizing other limitations requires careful case studies of dissimilar eruptive and confined events. This is particularly important, because the ion acceleration can only be quantified in rather powerful events, where gamma-ray line emission can be detected. The electron acceleration can be detected in a much broader range of flare sizes, but the characterization of the nonthermal electron energy content is often limited because of uncertainty in quantification of the poorly constrained lowenergy cutoff in the nonthermal electron spectrum. A more reliable method of finding the low-energy cutoff has been proposed (Kontar et al. 2019) via a warm-target model, which, however, relies on a number of model assumptions.

Recently, Lysenko et al. (2018) described a class of early impulsive "cold" flares, where the direct plasma heating is weak or nonexistent, while most of the plasma thermal manifestations are driven by the impact of nonthermal electrons accelerated in the course of the flare. Given that the thermal emission from the cold flares is somewhat low, the nonthermal

X-ray emission dominates the spectrum down to low energies, which permits much lower low-energy cutoff values to be derived, compared with a typical flare, even from the cold-target fit. The thermal component can also be quantified much more conclusively in the cold flares compared with the normal flare. Indeed, a reasonably low temperature ( $\sim\!10\,\text{MK})$  component of the thermal plasma in a cold flare can be spatially resolved with extreme-ultraviolet (EUV) data and, thus, studied in much greater detail than the hotter flaring plasma visible in X-rays.

A few case studies of the cold flares reported that the cold flares originate as a result of an interaction between two magnetic flux tubes. For example, Fleishman et al. (2016) analyzed a cold flare with a delayed heating and found that the flare occurred owing to an interaction between two magnetic flux tubes with strikingly different sizes—one small and one big loop. However, in spite of this remarkable difference in the loop sizes, the nonthermal accelerated electrons divided between these two loops in comparable amounts. Intriguingly, the thermal response of these two loops on the comparable nonthermal electron impact was different, likely because of the dissimilar geometry of the loops. In contrast, Motorina et al. (2020) demonstrated that another nonthermal-dominated cold flare occurred owing to an interaction between two flux tubes with comparable sizes. In this case, the nonthermal electrons were also divided roughly equally between these two loops, which might indicate that the nonthermal electron partition between two interacting loops is controlled by local properties of this interaction, rather than the loop sizes. However, the thermal responses of those two loops were again different, likely because of differences in the thermal plasma properties in the loops just before the flare.

Here we investigate the SOL2014-02-16T064600 flare that shares a number of properties with the cold flares, although it does not pass the formal criterion for the early impulsive cold flares proposed by Lysenko et al. (2018). This event is a rare (perhaps the only) case when a rather simple flare with a "single-spike" impulsive phase was observed with IRIS, so the kinetic energy of turbulent and bulk plasma motions at the flaring loop footpoints could be quantified based on the spectral line analysis. A study of energy distribution, partitioning, and evolution is facilitated by a unique combination of the complementary data sources. However, some of the essential data sets have noticeable temporal gaps, which we attempted to fill with the data-constrained 3D modeling (similar to that described in Motorina et al. 2020).

We found that three distinct flux tubes are involved in the SOL2014-02-16T064600 flare. However, unlike the cold flares studied, two of these three flaring flux tubes do not show any evidence of a significant nonthermal component. The nonthermal electron population is only detectable in the largest and hottest loop; this loop showed thermal-to-nonthermal behavior consistent with the Neupert effect (Neupert 1968). The loops, however, demonstrate a noticeable preheating phase, with no signature of any nonthermal electron component. The estimated input of the nonthermal electron energy is insufficient to fuel the overall thermal response in this flare, thus favoring an additional mechanism of plasma heating. The kinetic energies of the bulk and turbulent motions in the flare footpoints estimated from the shift and width of the spectral lines appear to be much smaller than either the thermal or nonthermal energy of the flare.

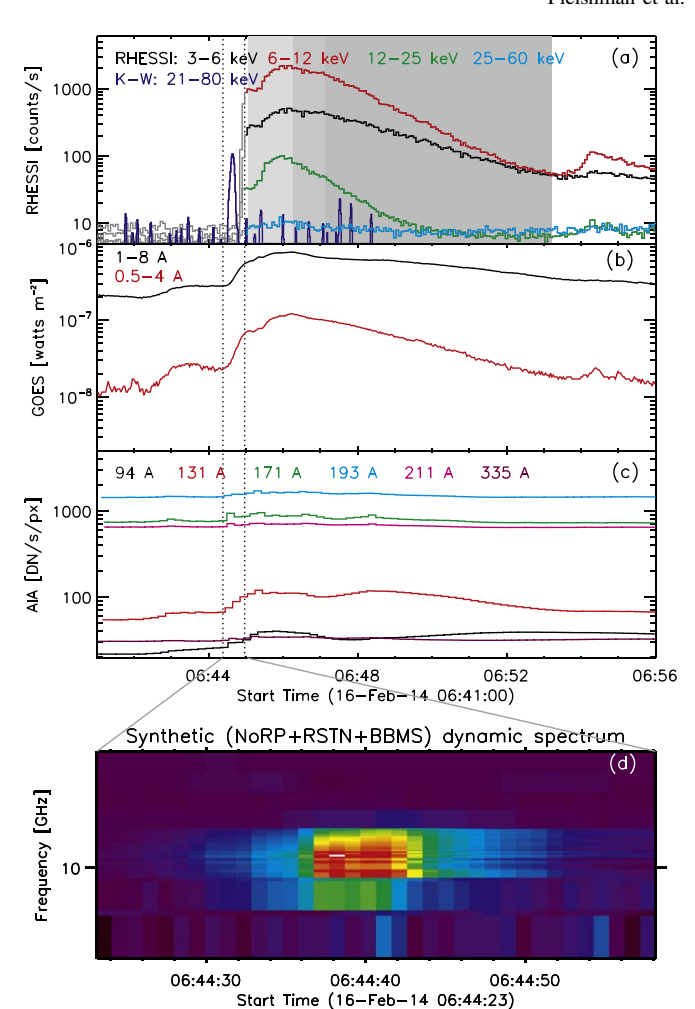


**Figure 1.** Overview of the 2014 February 16 flare. (a) RHESSI and Konus-Wind light curves; RHESSI light curves during the orbital night are shown in light gray. (b) GOES light curves. (c) AIA light curves obtained from the selected ROI (see Figure 3). (d) NoRP+RSTN+BBMS dynamic spectrum of the impulsive flare phase (the absolute peak of the radio flux density is 50 sfu). Vertical dotted lines indicate the impulsive phase shown in the bottom panel in the microwave emission. The light-gray area starting on 06:45:06 UT after the exit from the RHESSI night shows the 8 s fitted time intervals, the dark-gray area—the 12 s fitted time intervals, the darkest gray—the 20 s fitted time intervals of the RHESSI observations.

#### 2. Observations

The solar flare SOL2014-02-16T064600, GOES class C1.5, occurred at  $\sim$ 06:46 UT in active region (AR) 11974 with  $\beta\gamma$ -configuration located at W56S12 (cosine of heliocentric angle  $\mu=0.55$ ). The flare displayed a short impulsive profile with a single peak at  $\sim$ 06:44:38 UT in hard X-ray (HXR) above 20 keV and in microwave that lasted about 20 s.

## 2.1. Overview of the Instruments Used in the Analysis

The flare is observed with a unique combination of spaceand ground-based instruments throughout the entire electromagnetic spectrum from radio waves to HXRs; see Figure 1. Nevertheless, there are substantial gaps in these data, which we attempt to fill with 3D modeling.

In the HXR domain the event is observed by a few instruments: RHESSI (Lin et al. 2002), Konus-Wind (Aptekar et al. 1995; Pal'shin et al. 2014), and X-Ray Telescope (XRT; Golub et al. 2007) on board the Hinode mission (Kosugi et al. 2007). RHESSI

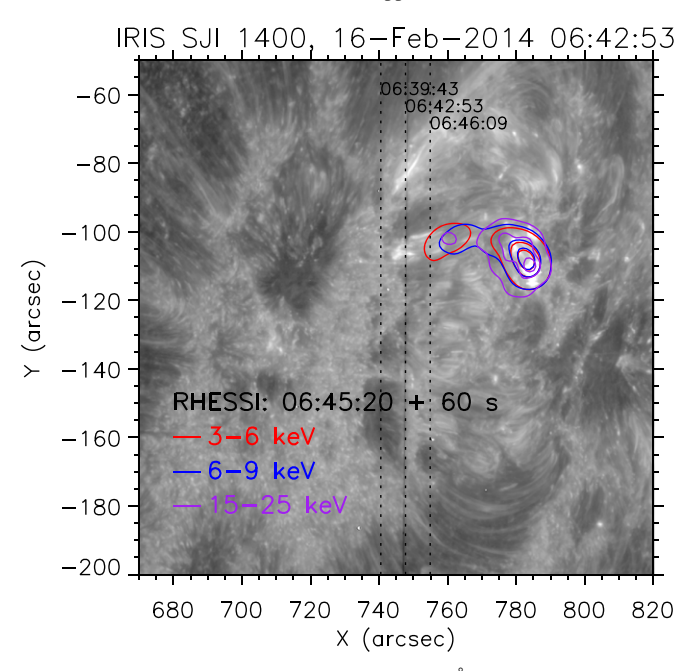


**Figure 2.** The background shows an IRIS SJ 1400 Å image taken at 06:42:54 UT, just as small brightenings were starting in the region. The RHESSI source, reconstructed at three different energy bins during a time interval of 60 s, overlays some of the brightenings. RHESSI contours are rotated 0.°2 clockwise about disk center as explained in Section 2.2. The vertical dotted lines indicate three different IRIS spectrograph slit positions with their times labeled, to show the motion of the spectrograph slit across the solar surface.

missed the impulsive phase owing to the orbital night and recorded only the thermal response phase (see Figure 1(a)). Konus-Wind was not in triggered mode, so only the low-resolution G1 (21–80 keV) light curve is available (dark-blue line, Figure 1(a)).

IRIS (De Pontieu et al. 2014) carried out a 400-step raster scan on 2014 February 16 from 06:16 to 07:19 UT. Each raster step took 9.5 s, consisting of an 8 s exposure time plus overhead, and encompassed an area of  $0.33 \times 174$ . This gives a total field of view (FOV) of  $141^{\prime\prime} \times 174^{\prime\prime}$ , with the caveat that the different slit positions are not obtained simultaneously. Fortunately, the IRIS slit was just above the region of activity at the time of the flare. For each slit position, IRIS recorded near-UV (NUV) and far-UV (FUV) spectra in several spectral lines that are described below. Figure 2 shows a context image and the IRIS slit positions at different time steps.

Soft X-rays are available from the Geostationary Operational Environmental Satellite (GOES; White et al. 2005; see Figure 1(b)), while optical and EUV data are available from Solar Dynamics Observatory/Helioseismic and Magnetic Imager (SDO/HMI; Scherrer et al. 2012) and SDO/Atmospheric Imaging Assembly (SDO/AIA; Lemen et al. 2012) respectively. The EUV light curves integrated over the region of interest (ROI; see Figure 3) are shown in Figure 1(c).

In the microwave domain the flare occurred in the time range covered by the Siberian Solar Radio Telescope (SSRT; Grechnev et al. 2003) and Nobeyama instruments. Nobeyama Radioheliograph (NoRH; Nakajima et al. 1994) finished observations a few minutes before the event. SSRT was in a transition mode to a new instrument: the data were taken, but no calibration has been available at the time of the flare to

produce images. The Solar Radio Spectropolarimeters (SRS; Muratov 2011) 2–24 GHz data were lost because of disk failure (A. T. Altyntsev 2021, private communication). The available microwave data set includes Nobeyama Radio Polarimeter (NoRP; Torii et al. 1979) data at a few frequencies, Radio Solar Telescope Network (RSTN; Guidice et al. 1981), and the Badary Broadband Microwave Spectropolarimeters (BBMS; Zhdanov & Zandanov 2015) data at 4–8 GHz; the combined dynamic spectrum is shown in Figure 1(d).

#### 2.2. X-Ray Data

HXR observations of the flare impulsive phase are only available in the Konus-Wind wide G1 channel covering the 21–80 keV range. The light curve with the time cadence of 2.994 s was recorded in the waiting mode, which we combine with the microwave light curves to evaluate the nonthermal electron escape time from the radio source.

RHESSI HXR observations with high temporal (2 s) and energy (1 keV) resolution provide information on electrons in the range from  $\sim$ 3 keV up to  $\sim$ 30–50 keV, and maps of X-ray sources with a spatial resolution of  $\sim$ 7" are only available in the decay phase of the flare. RHESSI data available after the terminator  $\approx$ 06:45 UT are used to produce images in the flare decay phase at a few spectral intervals between 3 and 25 keV using the CLEAN algorithm (Hurford et al. 2002) with clean beam width factor (CBWF) = 1.8; see Figure 3.

A loop-like structure connecting footpoints is observed during the impulsive peak with the Hinode/XRT using various filters. The RHESSI images were rotated by the roll angle rhessi\_roll\_angle = -0.2 using rhessi\_roll\_center = (0, 0) to co-align with these Hinode/XRT images, which are properly co-aligned with the SDO/AIA data.

GOES soft X-ray data are shown in Figure 1(b). There is a preflare enhancement well seen in both low- and high-energy channels at  $\sim$ 06:43 UT, which are roughly co-temporal with IRIS enhancement from box 1, shown in Figure 4, in 1400 and 1330 Å (see below for IRIS data) and with SDO/AIA enhancement, seen in time profiles in Figure 1(c) (see next section for SDO/AIA data analysis).

## 2.3. EUV: SDO/AIA Data

The standard EUV data set of the full solar disk is available from six SDO/AIA (94, 131, 171, 193, 211, 335 Å) coronal passbands. The AIA images with ~1."2 spatial resolution have been taken with 12 s cadence, calibrated using the aia\_prep.pro routine and normalized by the exposure time. We focus on the EUV emission from the ROI shown in Figure 3 to quantify the thermal energy and its evolution in the coronal part of the flare. We employ the differential emission measure (DEM) analysis technique applied to the entire ROI, as well as using the DEM maps with the methodology developed and applied by Motorina et al. (2020, hereafter Paper I) to a nonthermally dominated SOL2013-11-05T035054 solar flare. Some of the EUV images contain saturation artifacts. Unsaturated images with shorter exposure times are taken for the quantitative analysis of thermal energy of the flare.

#### 2.4. UV: IRIS Data

The IRIS data show activity (impulsive enhancements in a localized area) temporally coinciding with impulsive emission

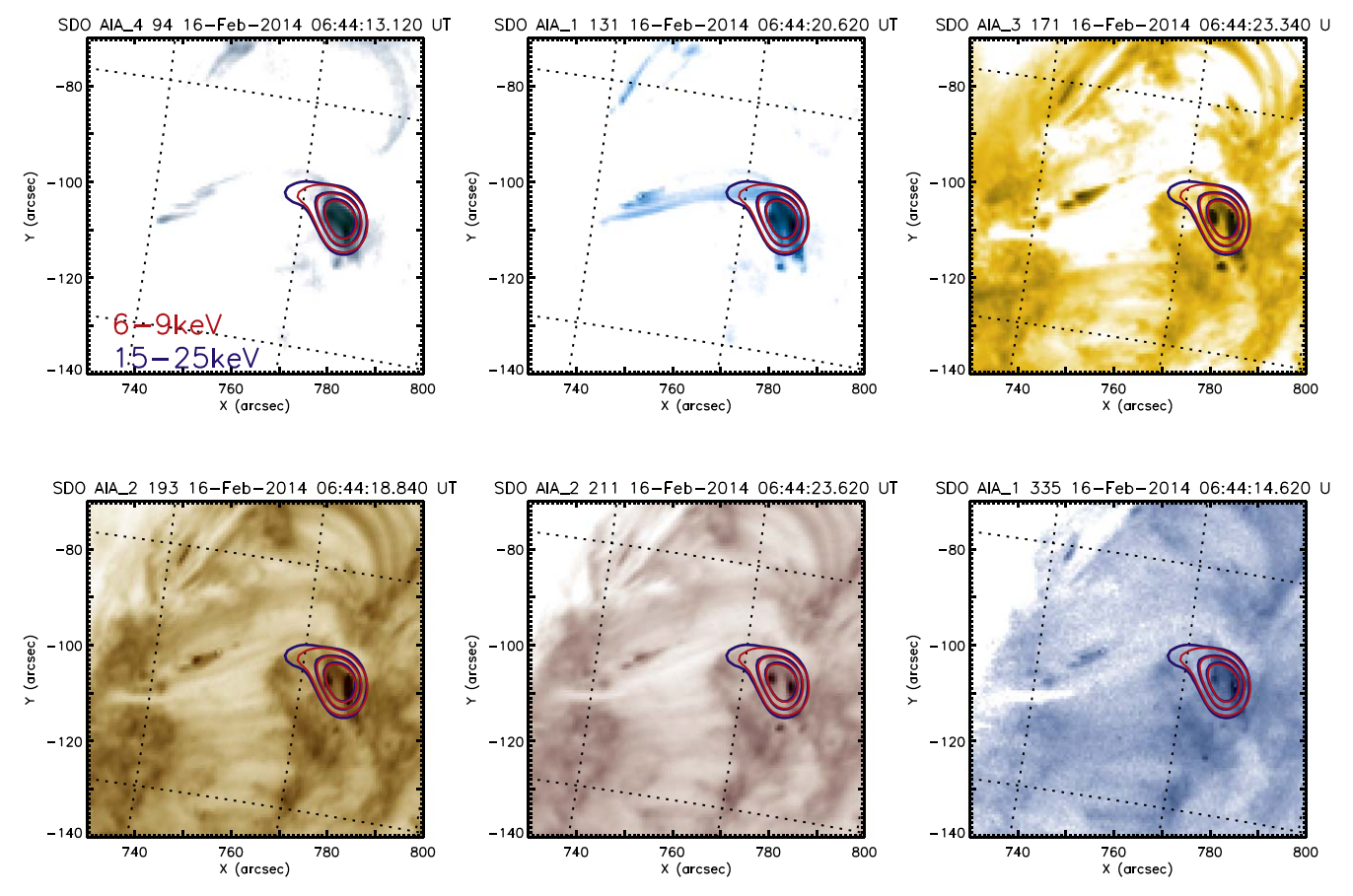


Figure 3. AIA maps of the 2014 February 16 flare with overlaid RHESSI CLEAN image (CBWF = 1.8) 30%, 50%, and 70% contours for 6–9 keV (red lines) and 15–25 keV (blue lines) for time interval 06:45:20-06:46:20 UT. For co-alignment the RHESSI roll angle rhessi\_roll\_angle = -0.2 has been applied to rhessi\_roll\_center = (0, 0).

from Konus-Wind and microwave. This is visible in the slit-jaw images with passbands around 1330 and 1400 Å, which were obtained at a cadence of about 20 s. Figure 4 shows that the enhancements of the more southern loop coincided temporally with the X-ray and microwave emission, while the northern loop brightened a few minutes earlier (while RHESSI was still in orbital night). The average intensity inside the two marked boxes is drawn in the right panels, for the IRIS 1330 and 1400 Å passbands.

The spectra allow us to probe the bulk velocities of the chromospheric and transition region plasma. We analyzed the spectral lines Si IV  $\lambda$ 1394, Si IV  $\lambda$ 1403, O IV  $\lambda$ 1399, O IV  $\lambda$ 1401, O IV  $\lambda$ 1405, and Fe XXI  $\lambda$ 1354, which form at different temperatures typical for the transition region or corona.

We verified that these spectral lines do not show irregularities (double peaks as, for example, observed in strong flares or supersonic flows) in our FOV and fitted a Gaussian function, with a central wavelength  $\lambda_0$  and FWHM  $\Delta\lambda$ , to each pixel for each spectral line to determine their Doppler velocities and Doppler widths and thus to quantify the kinetic energy of the plasma flows and turbulent motions.

#### 2.5. MW Data

As mentioned, there are no microwave imaging data for this event. Only total power (spatially integrated) spectroscopic data are available from several instruments, including NoRP (with a significant flux at 3.75 and 9.4 GHz and a weak signal at 17 GHz), RSTN (at 2.8, 5, 8.8, and 15.4 GHz), and BBMS

data at 4–8 GHz. These data were combined in a single synthetic dynamic spectrum (see Figure 1) as described in Lysenko et al. (2018). The dynamic spectrum and single-frequency light curves are employed in conjunction with the Konus-Wind light curve and the 3D model of the flare to constrain the nonthermal energy deposition in this flare.

#### 3. Thermal Plasma

# 3.1. Thermal Plasma Diagnostics with RHESSI

Given that RHESSI data are only available after the Konus-Wind impulsive peak is over, our expectation is to employ RHESSI spectroscopy to quantify the hottest thermal component of the flaring plasma using OSPEX.<sup>8</sup> The spectral fits were applied to the background-subtracted data (detectors 1, 4, 5) every 8 s from 06:45:06 to 06:46:18 UT, every 12 s for the interval 06:46:18–06:47:30 UT, and every 20 s for the 06:47:30–06:53:10 UT time interval for better statistics (the intervals are respectively highlighted by light-, dark-, and darkest-gray areas in Figure 1(a)).

We attempted a two-temperature fit in the 3–17 keV range, which returned a cool ( $T \sim 10 \, \text{MK}$ ) and a hotter ( $T \sim 25 \, \text{MK}$ ) component. However, uncertainties of the cool component parameters are very large, likely because RHESSI calibration is unreliable below  $\sim 6 \, \text{keV}$ . In addition, the  $\chi^2$  metrics were unacceptably high, due mainly to high residuals in the 3–7 keV

<sup>8</sup> For documentation see https://hesperia.gsfc.nasa.gov/rhessi3/software/spectroscopy/spectral-analysis-software/index.html.

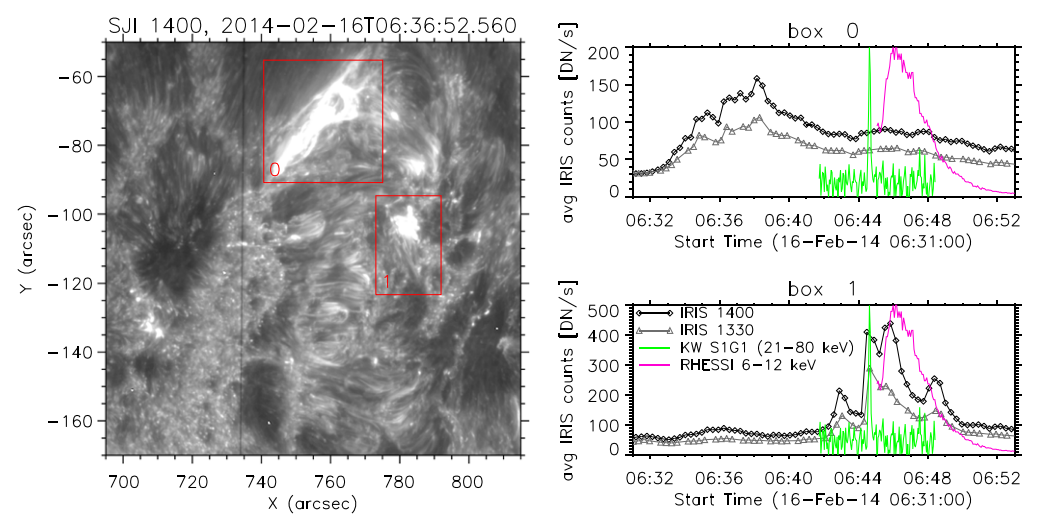


**Figure 4.** Temporal evolution of IRIS intensities. The red boxes in the left panel show the areas whose IRIS SJ intensities were averaged to produce the light curves in the right panels. It is visible that the northern loop brightened in both 1330 and 1400 Å around 06:38 UT, when RHESSI was still in orbital night (and GOES did not show any significant enhancement), while the southern loop brightened around 6:45 UT coincident with the emission from other wavelengths. The RHESSI and Konus-Wind data are integrated over the whole solar disk and are shown normalized to the plot window.

range. Thus, we only employ the hot component parameters ( $T2_{RHESSI}$ ) and EM2<sub>RHESSI</sub>) of this two-temperature fit, which are shown in dark green in Figure 6.

To cross-check these results, we attempted an isothermal plus thick-target spectral model fit in the 7–25 keV range, which resulted in a better  $\chi^2$  metric ( $\chi^2 < 3$ ). Two examples of the RHESSI fits, shown in Figure 5, indicate that the nonthermal component is either very weak or nonexistent. The time evolution of the fit parameters is shown in Figure 6. The thermal part of the fit resulted in the well-constrained temperature (green histogram in panel (a)) and emission measure (EM; green histogram in panel (b)) consistent with those derived from the two-temperature fit (dark-green lines).

The nonthermal component, even though it appeared to be needed to return acceptably good fits, has large uncertainties of the total integrated electron flux  $F_0$  (panel (c)), the low-energy cutoff  $E_c$  (panel (d)), and the spectral index  $\delta$  of the electron distribution function above  $E_c$  (panel (e)). These figures confirm that there is a marginal, if any, nonthermal component in the RHESSI data.

The RHESSI spectral model fits are used to quantify the thermal energy of the hottest component of the flaring plasma similarly to the estimate reported in Paper I. The only distinction is that now we cannot estimate the hot loop volume from data directly. Instead, we rely on the loop volume (Loop II,  $V_{\rm II} = 7.75 \times 10^{26} \, {\rm cm}^{-3}$ ; see Table 1) determined from the 3D model devised in Section 5.

#### 3.2. Thermal Plasma Diagnostics with SDO/AIA

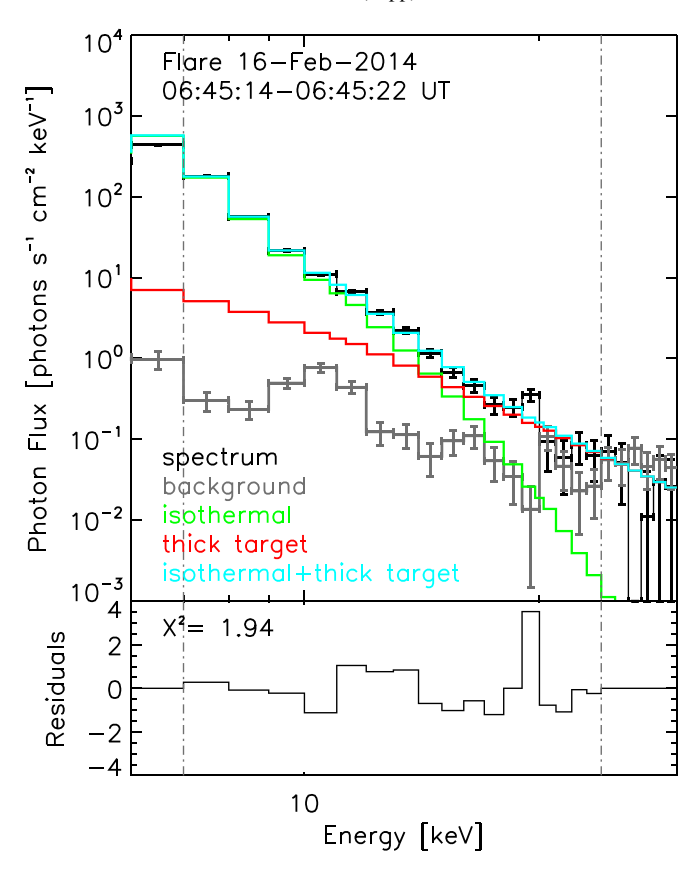
SDO/AIA observations are used to characterize plasma at temperatures 0.5–25 MK. To infer EM and temperature, we first calculate the DEM (cm $^{-5}$  K $^{-1}$ ) using a regularization technique (e.g., Tikhonov 1963). The total EM, EM<sub>AIA</sub> (cm $^{-3}$ ), and mean temperature,  $\langle T_{\rm AIA} \rangle$ , obtained from DEMs $^{9}$ 

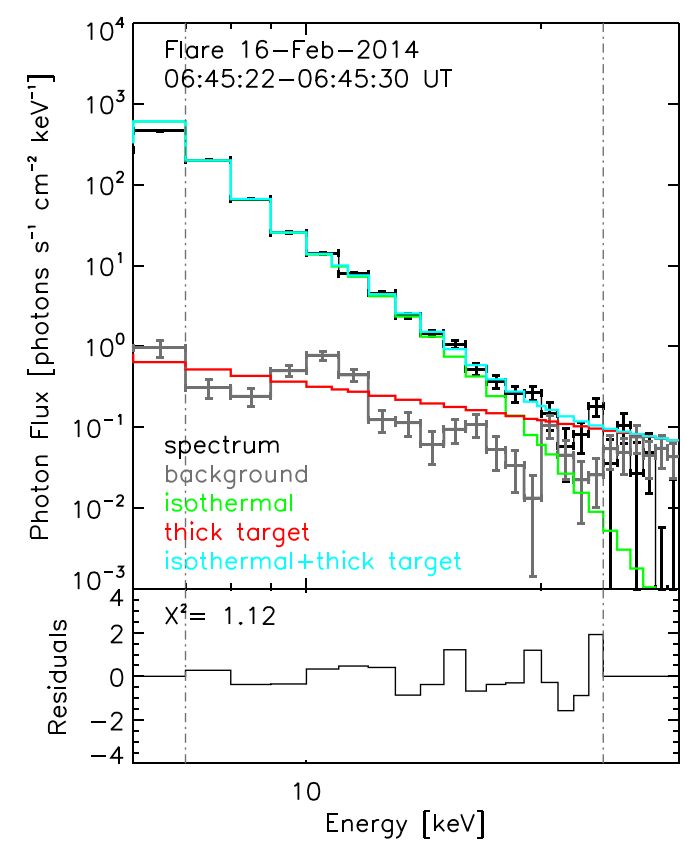
calculated from the ROI (see Equations (1)–(2) in Paper I) are shown in Figure 6. The saturation effects, including a secondary saturation (blooming), are within the errors. Figure 6 shows the evolution of  $EM_{AIA}$  and  $\langle T_{AIA} \rangle$  with the minimum preflare EM subtracted. After the HXR impulsive peak, shown by the Konus-Wind light curve, both the EM and temperature increase. Similar to the 2013 November 5 solar flare studied in Paper I, the values obtained from RHESSI and SDO/AIA are different from each other, which could mean that the two instruments see different sources with different temperatures.

Applying the regularized inversion code to the SDO/AIA data (Hannah & Kontar 2012, 2013), the DEM maps have been created using the methodology described in Section 2.3.2 of Paper I. The DEM maps are then used to calculate the EM maps  $\mathrm{EM}_{ij}^{\mathrm{AIA}}$  (cm<sup>-3</sup>), the mean temperature maps  $\langle T_{ij}^{\mathrm{AIA}} \rangle$  (K), and the thermal energy density maps  $w_{ij}^{\mathrm{AIA}}$  (erg cm<sup>-3</sup>) for all (i,j) pixels.

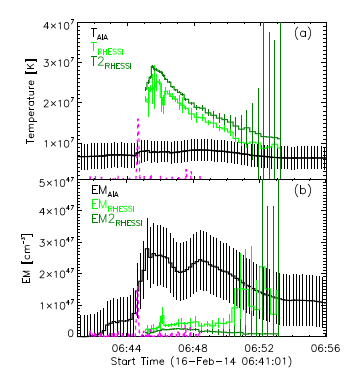
The 3D modeling of the flare described in Section 5 shows that the essential contribution to the EUV images comes from relatively cold and dense Loop I (see Figure 11 Table 1). Thus, to estimate the thermal energy density  $w_{ij}^{AIA}$ , the adopted length along the line of sight (LOS) has been taken as a characteristic diameter of the modeled Loop I (see Table 1), which is  $l_{\rm depth} = 2r \approx 3.8 \times 10^8$  (cm). The values  $EM_{ij}^{\rm AIA}$ ,  $\langle T_{ij}^{\rm AIA} \rangle$ , and  $w_{ij}^{AIA}$  are calculated using Equations (3)–(5) (Paper I) and are demonstrated along with the chi-squared ( $\chi^2 < 2$ ; bottom left panel) in the animated version of Figure 7. Figure 7 shows the 29th time interval (06:46:37–06:46:49 UT) of the animation. The mean temperature is close to 12-14 MK during the flare, while the EM and the thermal energy density evolve dramatically. The saturation effects become visible after 06:45:01 UT, just after the nonthermal HXR peak time. A distinct boundary between two temperatures ( $\sim$ 8 and  $\sim$ 12 MK) is seen in the  $\langle T_{ij}^{\rm AIA} \rangle$  maps. We interpret this as a projection effect when, due to the complexity of the flare loop structure, hot Loop II (reddish in Figure 7, top left panel) projects on cooler Loop I (greenish). Note that the (pre)heating takes place in both loops (I and II) before the impulsive energy release, seen in the microwave and Konus-Wind data.

The solar plasma DEM analysis employs the CHIANTI database, which assumes the ionization equilibrium. The assumption might be incorrect in the case of the impulsive phase of the flare, when plasma is transitioning to equilibrium. The coronal elemental abundances are used by default. This might be incorrect if evaporated chromospheric plasma dominates the flare thermal response.





**Figure 5.** Two examples (top: 06:45:14–06:45:22 UT; bottom: 06:45:22–06:45:30 UT) of RHESSI data (in black) and fits (in light blue). The background is shown in gray. The fit components are color-coded as indicated in the panels. The residuals are shown in the lower panels of these two plots.



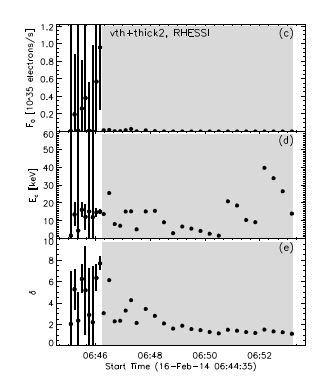


**Figure 6.** Temporal evolution of (a) T, (b) EM, and (c, d, e) nonthermal parameters for the 2014 February 16 flare. (a) RHESSI temperature of the hot flare component (green and dark-green histograms) from two spectral fits (see text) of the spatially unresolved full solar disk and AIA temperature of the cooler flare component (black histogram) from the ROI shown in Figure 3. (b) RHESSI (green and dark-green histograms) and preflare-subtracted AIA (black histogram) EM, inferred as described for panel (a). The red dashed histogram shows the Konus-Wind 21–80 keV light curve (arb. units). (c) Total integrated electron flux  $F_0$ , (d) low-energy cutoff  $E_c$ , and (e) spectral index  $\delta$  obtained from the RHESSI isothermal+thick-target fit. Vertical lines indicate the range of  $1\sigma$  error on the fits of the RHESSI data. The grayed-out area indicates the time range when the formal  $1\sigma$  errors exceed the plot ranges.

# 3.3. Thermal Plasma Diagnostics with IRIS

The coronal Fe XXI line is sensitive to plasma temperatures around  $10^7$  K. Signatures of Fe XXI are seen in flare loops, indicating the hot plasma. However, these signatures are weak (maximum of 1–2 DN s<sup>-1</sup>, compared to >10 DN s<sup>-1</sup> for other spectral lines), which precludes a reliable Gaussian fitting and thus a more quantitative analysis. This also precludes the use of this spectral line to estimate a coronal portion of the kinetic energy.

#### 4. Plasma Motions in the Flare

To quantify regular and random plasma motions of the flare, we focus on the spectral lines of Si IV ( $\lambda\lambda$ 1393.76 and 1402.77) and O IV ( $\lambda\lambda$ 1399.78, 1401.16, and 1404.78), which form at temperatures of  $10^{4.8}$  and  $10^{5.1}$  K, respectively (De Pontieu et al. 2014; Young et al. 2018). Note that this temperature range pertains to the flare footpoints and does not capture the coronal portion of the flare. Thus, these data quantify only a fraction of the total kinetic energy in the flare.

## 4.1. Bulk Plasma Velocity

Gaussian fitting allows us to determine the displacement of the Gaussian peak value  $\lambda_0$  from the expected rest-frame wavelength  $\lambda_{ji}$  of the transition between the levels i and j, which yields the bulk velocity due to the Doppler effect:

$$\frac{v_{\text{bulk}}}{c} = \frac{\lambda_0 - \lambda_{ji}}{\lambda_{ji}},\tag{1}$$

where c denotes the speed of light.

The Doppler fitting of Si IV  $\lambda 1394$  is very reliable, with few exclusions necessary: about 5% of the pixels were below our selected cutoff for the noise (1.25 DN s<sup>-1</sup>) and were therefore excluded. Furthermore, we excluded pixels with cosmic rays, spikes, or defects (based on the fitted FWHM  $\Delta\lambda$ ), amounting to 2% of the FOV.

Table 1 Summary of the 3D Model

Parameter	Symbol, Units	Loop I	Loop II	Loop III
Geometry:				
Length of the central field line	l, cm	$1.448 \times 10^{9}$	$6.345 \times 10^9$	$2.535 \times 10^{9}$
Reference radius of the flux tube at loop top	r, cm	$1.9 \times 10^{8}$	$1.52 \times 10^{8}$	$1.52 \times 10^{8}$
Model volume, $\left[\int n_0 dV\right]^2 / \int n_0^2 dV$	V, cm <sup>3</sup>	$7.27 \times 10^{25}$	$7.75 \times 10^{26}$	$4.03 \times 10^{25}$
Thermal plasma:				
Emission measure, $\int n_0^2 dV$	EM, cm <sup>-3</sup>	$8.91 \times 10^{46}$	$1.57 \times 10^{46}$	$2.58 \times 10^{46}$
Mean number density, $\int n_0^2 dV / \int n_0 dV$	$n_{th}$ , cm <sup>-3</sup>	$3.5 \times 10^{10}$	$0.45 \times 10^{10}$	$2.53\times10^{10}$
Temperature	T, MK	9	25	10
Instant total thermal energy	$W_{th}$ , erg	$0.95 \times 10^{28}$	$3.61 \times 10^{28}$	$4.23 \times 10^{27}$
Nonthermal electrons:				
Total electron number	$N_b$ , cm <sup>-3</sup>	•••	$2.41 \times 10^{35}$	
Low/high-energy cutoff	$E_0$ , MeV	•••	0.01/2	
Spectral index	$\delta$		3.9	
Instant total nonthermal energy	$W_{nth}$ , erg		$5.87 \times 10^{27}$	

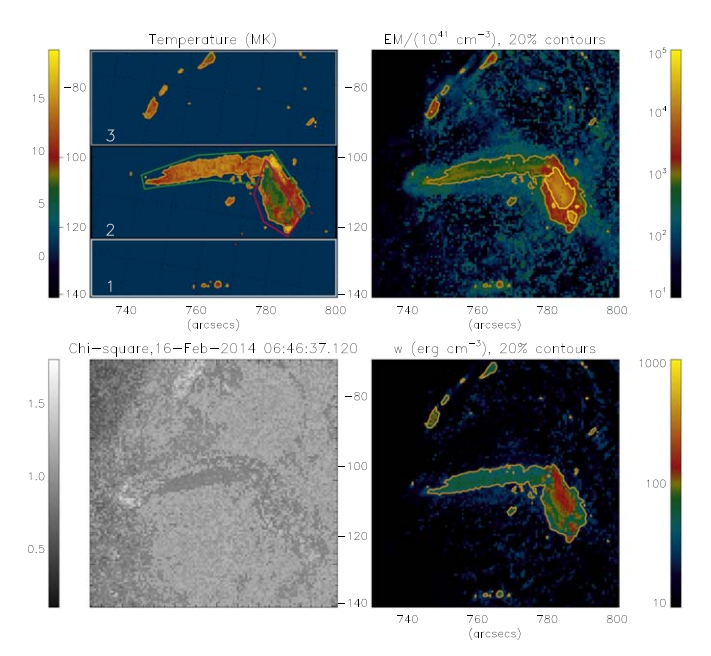


**Figure 7.** Spatial distributions of plasma parameters derived from SDO/AIA data with the regularized DEM inversion technique. The temperature map is shown in the top left panel, the EM map is in the top right panel, the chi-squared map is in the bottom left panel, and the thermal energy density map is in the bottom right panel. This figure represents the 29th time interval (06:46:37–06:46:49 UT) of the animation that shows the entire evolution of the flare thermal parameters. To aid the eye, in each time frame we plot the contours that indicate 20% of the thermal energy density peak (in orange) and 20% of the EM peak (in yellow). The temperature map is plotted only within the orange contour. An animation is included with this figure. The video shows the entire flare event starting on 2014 February 16 at 06:41:01 UT and ending the same day at 06:56:01 UT. The video duration is 19 s.

(An animation of this figure is available.)

Figure 8 shows enhanced Doppler widths at the location of the RHESSI source in Si IV  $\lambda 1394$  and also in the more northern loop (0.5 Å vs. 0.2–0.3 Å in the quiet Sun). Nearly identical values were obtained from Si IV  $\lambda 1403$  (therefore not shown). The Si IV Doppler velocities were not very noteworthy and ranged between  $\pm 20~{\rm km~s^{-1}}$ , which is a common range also in the quiet Sun as shown in the left panel. Excluded pixels are shown in black for the Doppler widths and with a value of zero (gray) for the Doppler velocity.

#### 4.2. Turbulent Plasma Velocity

The total line broadening depends on three quantities: the thermal line width  $\frac{2k_BT_{\rm ion}}{M_{\rm ion}}$  (km s<sup>-1</sup>), the instrumental broadening  $\sigma_I$  (km s<sup>-1</sup>), and the nonthermal line width  $\nu_{\rm turb}$  (km s<sup>-1</sup>). Thus, the FWHM  $\Delta\lambda$  of a spectral line in units of Å can be written as

$$\Delta \lambda = \frac{\lambda_0}{c} \sqrt{4 \ln 2 \left( \frac{2k_B T_{\text{ion}}}{M_{\text{ion}}} + v_{\text{turb}}^2 + \sigma_I^2 \right)}.$$
 (2)

The IRIS instrumental broadening was determined both by lab measurements (Tian et al. 2014) and by measuring the O I  $\lambda 1355.598$  line (De Pontieu et al. 2014) and yielded for the spectral range around the Si IV line about 30 mÅ (6.4 km s<sup>-1</sup>). The thermal broadening for Si IV is 50 mÅ ( $\approx 11 \text{ km s}^{-1}$ ), and for O IV it is 90 mÅ ( $\approx 19 \text{ km s}^{-1}$ ).

Because of the better signal-to-noise ratio, we use the Si IV line to calculate the nonthermal line width based on its Gaussian fits, which allowed us to determine the total FWHM and solve Equation (2) for  $v_{\rm turb}$ . We caution that this is only an approximation because we derive the FWHM by fitting a single Gaussian, which may not be entirely accurate in some flare pixels (Jeffrey et al. 2016). A visual inspection of the spectra shows that this seems reasonable in most pixels, but there are pixels with broad asymmetric spectra, whose origin probably is a superposition of multiple atmospheric components, for example, multiple downflows of different velocities within one pixel. Such pixels lead to an overestimation of the turbulent velocities, and therefore our number given here is rather an upper limit.

# 4.3. Density Diagnostics Using O IV Lines

Several O IV lines are observed in IRIS's spectrum. They are generally weak, but they are visible in some locations, particularly around our flare loops. We carried out a similar Doppler fitting of the O IV  $\lambda 1401.156$  line, and in this case 73% of all pixels had to be excluded owing to being too noisy, and an additional 5% because of cosmic rays or the fitted FWHM being below our cutoff (50 mÅ). Nevertheless, the good pixels appeared to have very similar properties to Si IV

<sup>10</sup> https://iris.lmsal.com/itn38/

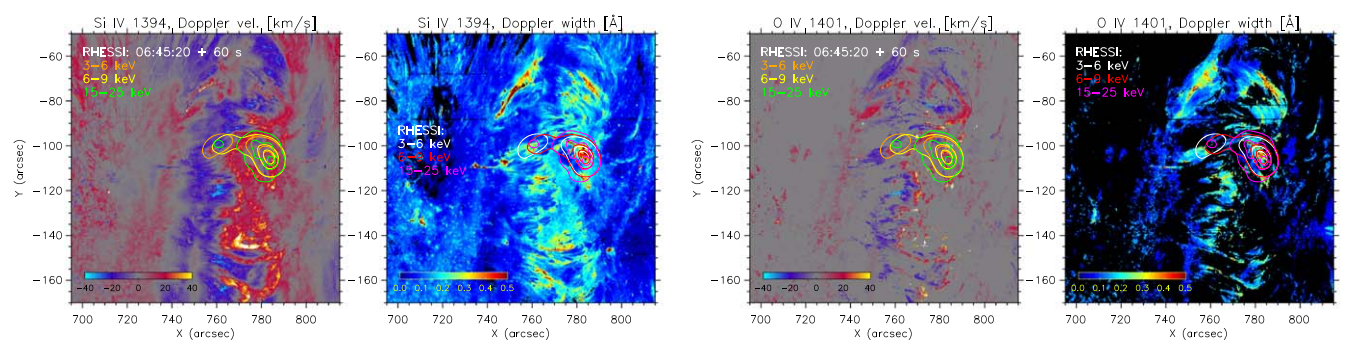


Figure 8. Left panel: Doppler velocities, obtained from Gaussian fitting to the Si IV  $\lambda$ 1394 line. Bad pixels (noise below cutoff, cosmic rays, etc.) were set to zero velocity. Negative (blue) values indicate the blueshift (away from the Sun; positive (red) values indicate the redshift (toward the Sun). Second panel: FWHM of the Gaussian, representing the Doppler widths. Bad pixels are shown in black. The flare locations show enhanced Doppler widths, but no particularly unusual Doppler velocities. Third and fourth panels: similar plots for O IV where many more pixels are below the noise limit. The pixels above the noise limit show similar properties to the corresponding ones in Si IV  $\lambda$ 1394.

 $\lambda$ 1394. We therefore later use the Si IV  $\lambda$ 1394 Doppler velocity as a proxy for the O IV  $\lambda$ 1401.156 Doppler velocity.

Line intensity ratios of several O IV lines around 1400 Å can be used as diagnostics for electron densities in the range of  $10^9 - 10^{11} \,\mathrm{cm}^{-3}$  and weakly up to  $10^{12} \,\mathrm{cm}^{-3}$  (e.g., Flower & Nussbaumer 1975; Doschek et al. 2016; Polito et al. 2016; Young et al. 2018). Our goal is to estimate the electron density near the RHESSI source to be able to calculate the kinetic energy density. We use the ratio of the O IV  $\lambda 1399.8/\lambda 1401.2$ lines because it is least blended as shown in the example spectra in Figure 9. A drawback is the low intensity of the  $\lambda$ 1399.8 line, which is below the noise level for many pixels. We integrate over a range of 0.8 Å (indicated with blue lines in Figure 9) and apply selection criteria on the integrated intensity and the ratios to exclude noise, cosmic rays, or unusual spectra. We visually verified that the remaining spectra show regular line profiles and produce ratios in the expected range (0.18–0.42). We assumed thermal and ionization equilibrium to apply this density diagnostic. Although it is difficult to firmly justify, considering the weakness of the flare, plus that the slit crossed it after its impulsive phase, we do not expect big errors with this assumption. Figure 10 shows our resulting ratios and densities. The ratios (middle panel) can only be determined near the flare site. Black indicates a ratio near zero, meaning that the  $\lambda$ 1399 line is below the noise level, while white pixels indicate that one of the exclusion criteria was met, which includes too small integrated intensities and abnormal ratios, e.g., due to cosmic rays or large Doppler velocities and thus blending of the Si IV line. Even though the accuracy of this method can be debated, mostly because of the low O IV signals in the present observation, the figure shows that the densities of our ROI are around  $10^{11}$ – $10^{12}$  cm<sup>-3</sup> with few (measurable) densities below those values.

### 5. Modeling and Model Validation

Using the data described in the previous section, we are in the position to quantify the thermal and kinetic energies, but we cannot quantify the nonthermal energy (deposition) with the available data alone; see Paper I. Here, to estimate the nonthermal electron component in the flare, we are forced to combine the incomplete microwave and Konus-Wind data with 3D modeling of the flare based on nonlinear force-free field (NLFFF) reconstruction. This reconstruction has to be initiated

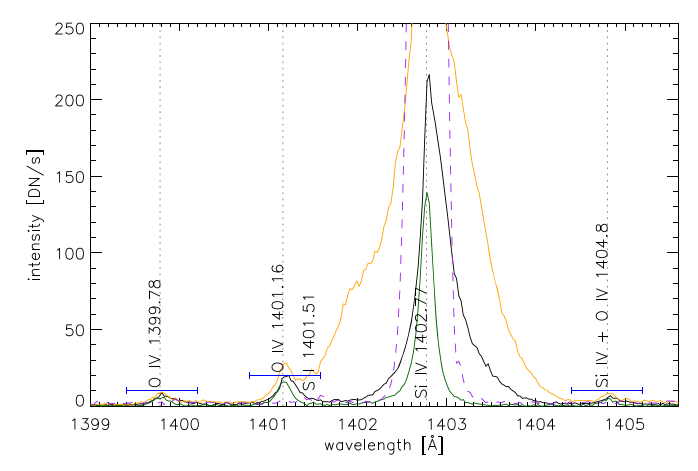


**Figure 9.** Spectra of example pixels (different colors) showing the O IV lines near 1400 Å. The blue bars indicate the wavelength range over which the intensity was integrated to determine the total line intensity used to calculate the line ratios. It is visible that the O IV lines are weak and can often be below the noise level. In the case of large velocity flows, the  $\lambda 1401.16$  line can be blended by the nearby Si IV line, further complicating the determination of its integrated intensity.

with the photospheric vector boundary condition available for this event from both SDO/HMI and Hinode/SOT.

### 5.1. Model Creation via the Pipeline

In this study we employed the automated model production pipeline (G. M. Nita et al. 2021, in preparation) based on the NLFFF extrapolation code (Fleishman et al. 2017a) initiated with an SDO/HMI vector magnetogram taken at 06:34:12 UT. Visual inspection of automatically downloaded base maps does not reveal any apparent inversion or  $\pi$ -disambiguation artifact, so the model did not require any manual correction (see Anfinogentov et al. 2019).

### 5.2. Selection of the Flaring Loops

The NLFFF 3D magnetic data cube is imported in the modeling tool GX Simulator (Nita et al. 2015, 2018), where the flaring flux tubes are interactively created. The GX Simulator functionality permits computation (and visualization) of selected magnetic field lines such as to match available flare images. In our case, we used only images of thermal emission obtained from RHESSI data at various energy ranges and also

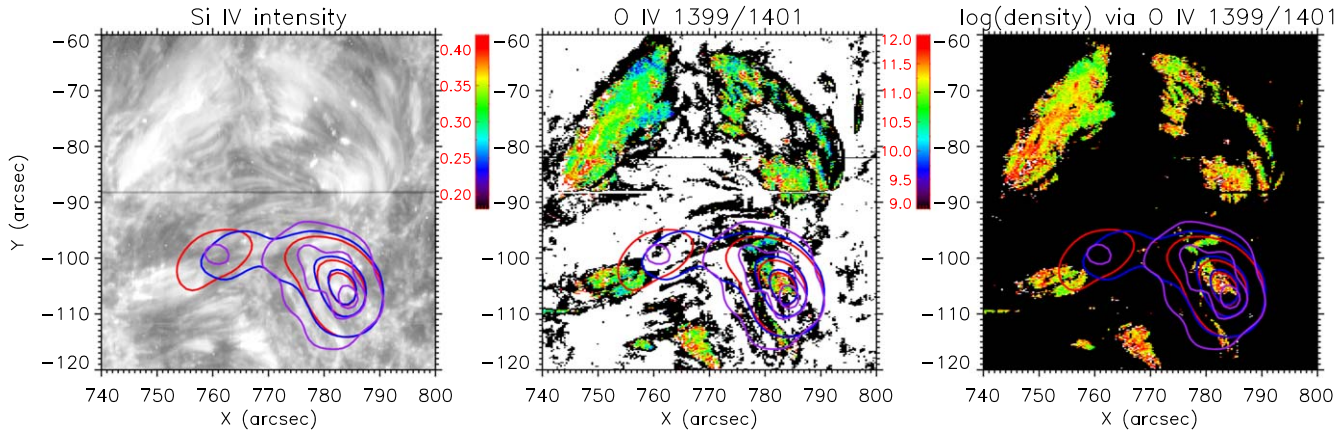


**Figure 10.** Left: Si IV intensity showing the flare loops and overplotted RHESSI contours (identical color-coding to Figure 2). Middle panel: ratio of integrated intensities of the O IV  $\lambda$ 1399.8/ $\lambda$ 1401.2 lines. White and black pixels met one of the exclusion criteria (see text). Right panel: ratio converted to densities. The color bar indicates the log of the densities, which can range from  $10^9$  to  $10^{12}$  cm<sup>-3</sup>.

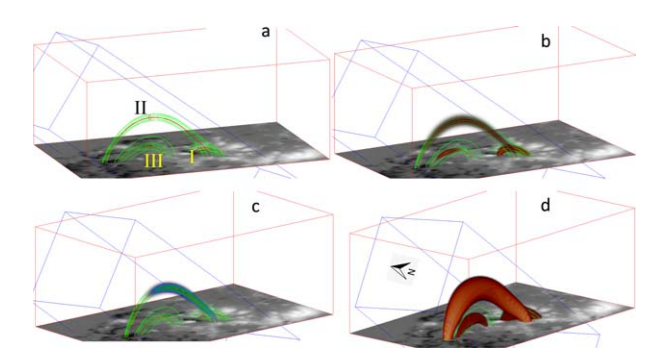
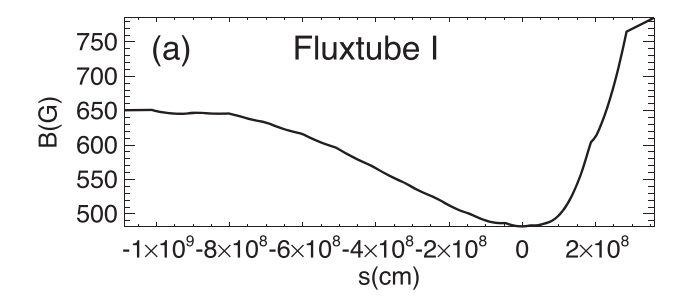


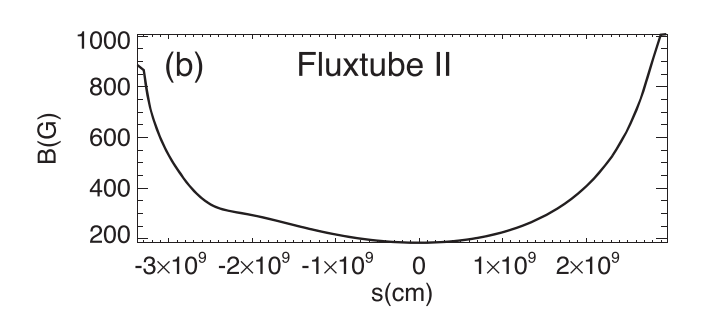
**Figure 11.** 3D model with three flux tubes (closed loops), which are labeled with their numbers (I–III) in panel (a). (a) magnetic flux tubes; (b) distribution of thermal number density in the flux tubes; (c) distribution of nonthermal number density in the flux tubes (in Loop II only); (d) distribution of the temperature in the flux tubes. Red lines indicate the outer borders of the magnetic data cube, where the coronal magnetic model has been computed. The bottom of the data cube shows the photospheric LOS magnetogram. The blue lines outline the scan box from the outer (upper left) boundary of which the emissions are computed within the GX Simulator. The arrow in panel (d) shows the solar north direction. An animation is included with this figure. The video sequentially shows 360° rotations of panels (b), (c), and (d). The video duration is 9 s.

(An animation of this figure is available.)

EM maps obtained from the DEM/AIA maps. This yielded two distinct flux tubes: Loops I and II; see Figure 11 and Table 1.

Guided by the thermal plasma parameters derived from the OSPEX fit to the RHESSI data and EM maps obtained from AIA data, we succeeded in reproducing most of the imaging data, except for the eastern source in the RHESSI 3–6 keV image. To reproduce this source, we created one more flux tube (Loop III) filled with a relatively cool plasma (10 MK). The magnetic field profiles along the central (reference) field lines in all three of these loops are shown in Figure 12. With these three loops all thermal images are closely reproduced in the model; see Figure 13. Loop III projects on the IRIS Fe XXI source, indicative of the 10 MK plasma there; see Figure 13. Figure 13 also illustrates the effect of the RHESSI point-spread function (PSF), which smears contributions from various thermal flux tubes out, producing a (misleading) visual impression that only a single loop is present.





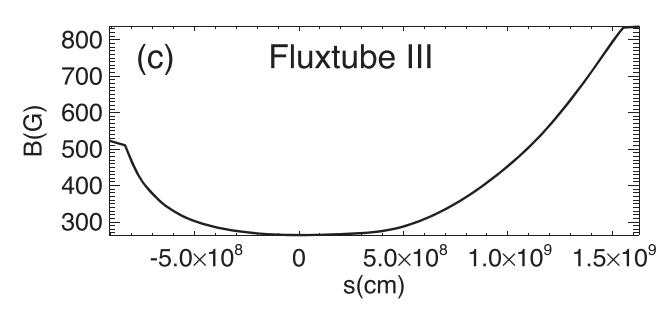


**Figure 12.** Distributions of the absolute value of the magnetic field along the spines of three flux tubes selected for 3D modeling of the flare.

# 5.3. Population of the Flaring Loops with Nonthermal Electrons

The next step of flare model creation is populating the flux tubes with nonthermal electron components, which are ideally guided by images of nonthermal emission. However, such images are not available in our case; thus, we are forced to employ the only available microwave spectral data. To be

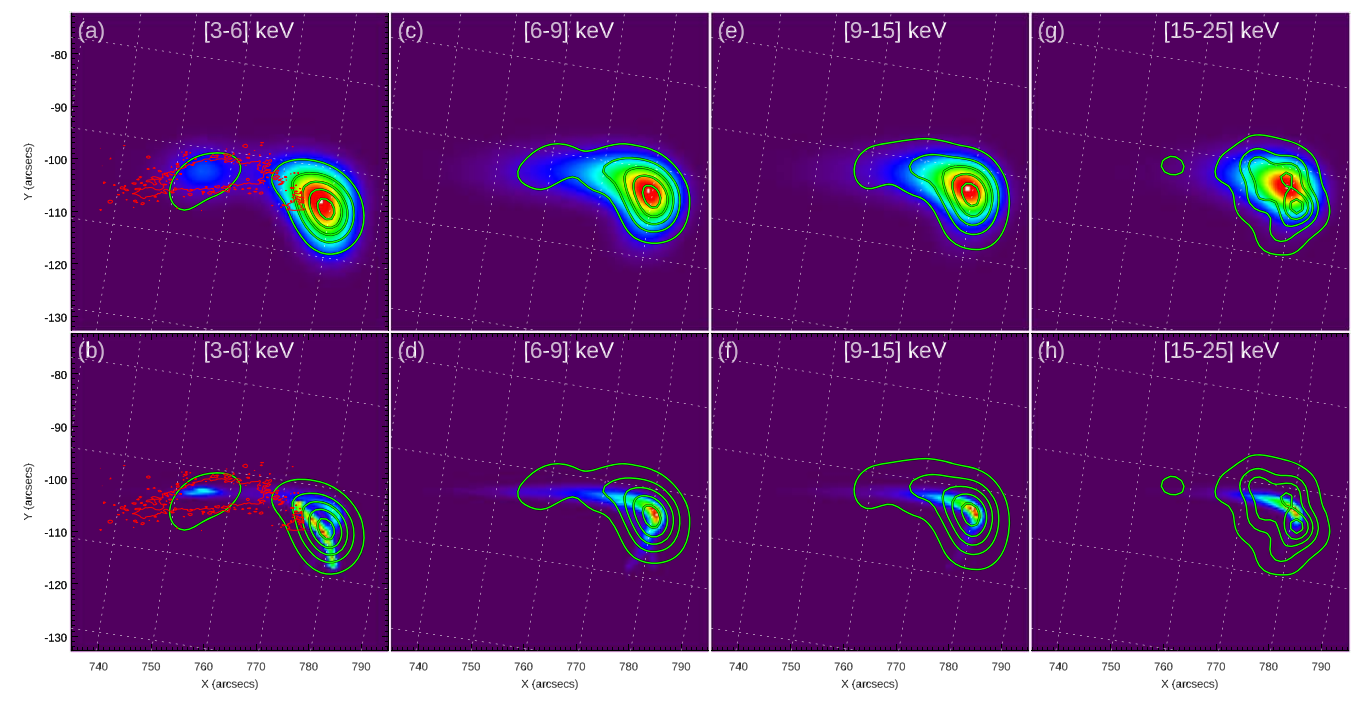


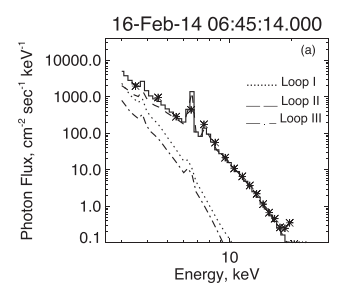
Figure 13. GX Simulator–generated X-ray images from the three-loop model integrated over the ranges 3–6 keV, 6–9 keV, 9–15 keV, and 15–25 keV, convolved with the RHESSI PSF (first row) and nonconvolved (second row). The RHESSI CLEAN 10%, 30%, 50%, 70%, and 90% contours (green lines) at the same energy ranges are overplotted. In addition, the integrated IRIS intensities at 1353.9–1354.15 Å (Fe XXI) are shown in panels (a) and (b) (magenta). The bright Fe XXI emission comes from Loop 3, as well as the eastern RHESSI source at 3–6 keV. The bottom row shows cleanly three distinct contributions from three model loops. These contributions are smeared out by the finite spatial resolution and so are not distinguishable in the top row. RHESSI images are synthesized for the time range 06:45:20–06:46:20 UT. The IRIS image is for the time range when the slit crossed this region, which lasted about 15 minutes. To co-align the RHESSI and model maps, we applied the RHESSI roll angle rhessi\_roll\_angle = -0.2 to rhessi\_roll\_center = (0, 0), similarly as in Figure 3. This roll angle is equivalent to y shift of -4. This is applied to 3 keV maps and to nonconvolved maps, while  $\Delta x = 1$ ",  $\Delta y = -2$ " was applied to higher-energy convolved maps. This additional mismatch might be provided by an error of the connectivity reconstruction in the NLFFF model (Fleishman et al. 2019), or a minor inaccuracy in the spatial distribution of the thermal plasma in loop 2 (longest, hottest one).

specific, we focus on the microwave emission peak time at 06:44:41 UT.

There could be ambiguity about how exactly to distribute nonthermal electrons between three available thermal loops of our model given the absence of the relevant images. Moreover, the bulk of the flaring microwave emission from a flare can come from entirely different flux tubes, not visible as a thermal source (Fleishman et al. 2017b; Kuroda et al. 2018).

Luckily, for the given flare this ambiguity can be largely removed owing to strong sensitivity of the gyrosynchrotron spectrum to the magnetic field in the emission source (Fleishman et al. 2020, Supplementary Materials including movie S2): the stronger the magnetic field, the larger the spectral peak frequency. Combining this property of the gyrosynchrotron spectrum with the dependence of its high-frequency slope on the nonthermal electron energy spectrum and of its low-frequency slope on the source geometry (Fleishman et al. 2020), we found that populating either Loop I or Loop III with a noticeable amount of nonthermal electrons results in overestimating the microwave emission at high frequencies and, simultaneously, underestimating it at the low frequencies.

This conclusion appears model independent and related only to the fact that the magnetic field is too high in those two loops: if we match the spectral peak frequency, then the model flux level is way too low; if we match the flux level (at a high frequency), then the spectral peak frequency is much higher than observed. After careful investigation, we concluded that an energetically dominant fraction of the nonthermal electrons



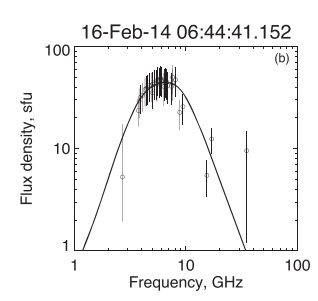


**Figure 14.** (a) Observed RHESSI X-ray spectrum for time interval 06:45:14–06:45:22 UT (asterisks) and the corresponding simulated spectrum (histogram) from the 3D model. Contributions from three distinct model loops are shown by various lines. (b) Same as panel (a), but for the radio domain with NoRP, RSTN, and BBMS data at 04:44:41 UT (circles) and the simulated microwave spectrum (black solid line). Only the total model spectrum is shown because contributions to the radio emission from Loops I and III are negligible. Note: the time frames selected for panels (a) and (b) are not the same because of RHESSI night during the impulsive flare phase.

must be located in Loop II;<sup>11</sup> see Table 1, with which we can nicely reproduce the synthetic microwave spectrum as shown in Figure 14. The model outlined in Table 1 is consistent with all available observational constraints and thus validated by the data.

With this model we can also check whether the presence of a modest nonthermal component derived from the RHESSI fit

<sup>11</sup> It would be desirable to estimate the upper limits of the nonthermal electrons in flux tubes I and III, but it is hard to do without imaging data. The only safe statement would be that those numbers are undetectably small versus Loop II numbers.

in Section 3.1 is consistent with the data. To this end, we populated flux tube II with nonthermal electrons consistent with the RHESSI fit and computed the microwave emission. We found that the microwave emission produced by this nonthermal electron population is below the 1 sfu level at all frequencies and thus not observable. Therefore, we cannot confidently exclude the presence of a nonthermal electron population as derived from the RHESSI fit even though the uncertainties of the associated parameters are rather large.

# 6. Energy Partitions and Evolution

In this section we use the model and the data analysis products described above to quantify energies, energy partitions, and evolution thereof.

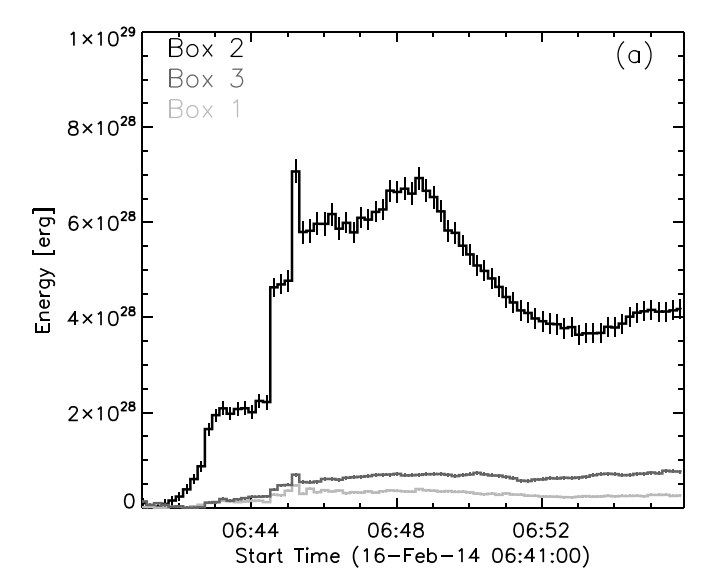
# 6.1. Thermal Energy Derived from EUV Data

The total AIA-derived thermal energy of the flare in the FOV is obtained from the spatial distribution of the thermal energy density  $w_{ij}^{AIA}$ , computed from the regularized DEM maps in Section 3.2, by adding up the contributions from all pixels in the FOV:

$$W_{\text{therm}}^{\text{AIA}}(t) = S_{\text{px}} \ l_{\text{depth}} \sum_{i=1}^{N_{\text{px}}} \sum_{j=1}^{N_{\text{px}}} w_{ij}^{\text{AIA}}(t) \text{ [erg]}.$$
 (3)

The animated Figure 7 shows that in addition to the evolution of the main flaring source, there is some dynamics in the top and bottom boxes (outlined in the figure by gray and light-gray contours). We cannot reliably conclude whether this dynamics is related to the flare or independent. To estimate contributions from those boxes to the thermal energy, we show them along with the one from the middle (black) box in Figure 15(a). The middle box uses the LOS depth  $l_{\text{depth}} = 3.8 \times 10^8 \, \text{cm}$ , which is comparable to the width of the loops, while two other boxes employ  $l_{\text{depth}} = 7.6 \times 10^7 \text{ cm}$ , because the dynamic features are only about 1" wide. The figure shows that the contributions from the top and bottom boxes are small compared with the main one; however, they display a behavior correlated in time with the main flaring box. This could indicate that the flaring process spreads out over a region larger than the main flaring loops. In what follows we, however, focus on the main flare region—the middle box.

Figure 15(b) displays further details of the thermal energy distribution and evolution within the middle (black) box in Figure 7. Here the green/magenta lines show the thermal energy computed for two different green/magenta ROIs in Figure 7. These two ROIs are selected such as to inscribe the two different flaring loops as closely as possible. Note that this loop separation cannot be perfectly done because one of the loops projects onto the other. The magenta and green symbols show the thermal energies computed by the volume integration of the thermal energy densities in flux tubes I and II, respectively. Although they agree with the data within a factor of two, they do not match each other perfectly. There are two possible causes of these mismatches: (i) the already-mentioned projection effect, and (ii) the ambiguity in determining the depth of the source, for which only a rough estimate is available from the data. Potentially, the values derived based on



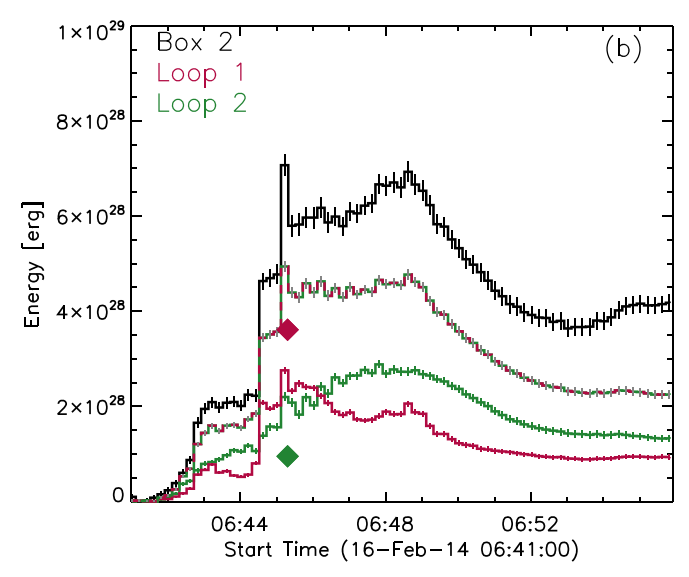


**Figure 15.** (a) Evolution of thermal energy computed from the DEM maps inside three boxes outlined by black, gray, and light-gray contours in Figure 7. (b) Components of the thermal energy inside the black (flaring) box in Figure 7: green/magenta lines correspond to green/magenta ROIs; the dashed green-magenta line shows the sum of them; the black line shows the result for the entire box (same as the black line in panel (a)). The red and green symbols indicate the model values of thermal energies in Loops I and II, respectively; see Table 1.

the 3D model are more precise, as they are free from the LOS ambiguity. The dashed green-magenta line shows the sum of those two contributions, while the black line shows the thermal energy from the entire middle (black) box. This suggests that there is some thermal flare energy outside the most distinct loops, even though the loops give dominant contributions to the thermal energy budget.

In all cases, a minimal preflare energy from the corresponding box or ROI was subtracted; for the middle (black) box this minimal preflare value is  $W_{\text{therm, min}}^{\text{AIA}} = 2.54 \times 10^{28}$  (erg), which comes from the nonflaring pixels in the FOV. Evolution of this energy (from the black box) is shown in Figure 16 in black. Its peak value is about  $7 \times 10^{28}$  (erg).

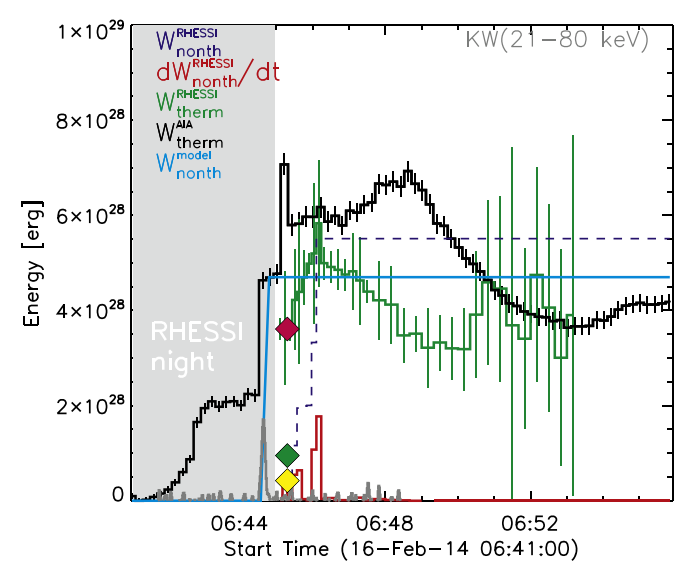


**Figure 16.** Evolution of energy components in the 2014 February 16 flare. The thermal energy  $W_{\rm therm}^{\rm RHESSI}$  (Equation (4)) computed using the thermal part of the RHESSI fits is shown in green, while the thermal energy  $W_{\rm therm}^{\rm RHESSI}$  (Equation (3)) computed from the middle/black box of the AIA DEM maps is shown in black. The grayed-out portion of the plot indicates the RHESSI night. The normalized Konus-Wind light curve indicating the flare impulsive phase is shown in magenta, while the red histogram shows the rate of RHESSI nonthermal energy deposition  $dW_{\rm nonth}^{\rm RHESSI}/dt$  (arb. units). The nonthermal energy input inferred from the validated 3D model is shown in a light-blue step function. The red, green, and yellow symbols indicate the model values of thermal energies in Loops I, II, and III, respectively; see Table 1. The cumulative nonthermal energy deposition  $W_{\rm nonth}^{\rm RHESSI}$  after the impulsive phase obtained using parameters of the nonthermal part of the RHESSI fits (Equation (6)) is shown with the dashed blue histogram.

# 6.2. Thermal Energy Constrained with X-Ray Data and 3D Modeling

To calculate the thermal energy detected by RHESSI, we use the EM and temperature obtained from the RHESSI fit (to be specific, we only employ here the single-temperature+thicktarget fit; see Section 3.1 and green lines in Figure 6; the alternative, two-temperature fit, yields very similar results):

$$W_{\text{therm}}^{\text{RHESSI}} = 3k_B T_{\text{RHESSI}} \sqrt{EM_{\text{RHESSI}} \times V} \text{ [erg]},$$
 (4)

where V is the volume of the corresponding thermal source. Here we use the model volume of Loop II from Table 1. The evolution of this energy is shown in Figure 16 in green; the peak value is about  $5 \times 10^{28}$  (erg).

We note that RHESSI is mostly sensitive to the hottest plasma within the FOV, namely, for emission from flaring Loop II in our case, which is also quantified by the AIA data in the previous section; see the green line in Figure 15(b). It is instructive to compare these two green curves. The RHESSI-derived thermal energy has a peak around 06:47 UT, where the temperature is the largest (about 30 MK), while the AIA-derived thermal density of this loop has a peak 1 minute later, when the plasma cooled down to  $\sim\!20$  MK or less. The two energies agree well after that. The reason of the mismatch between these energies at the early decay phase is the well-known fact that AIA is not sensitive to plasma above  $\sim\!20$  MK; thus, AIA-based thermal diagnostics underestimates the thermal energy of that hot plasma, to which RHESSI is the most sensitive.

#### 6.3. Bulk Kinetic Energy at the Flare Footpoints

Knowing the densities and the velocities, we can calculate the energy density  $w_{\text{bulk}}^{\text{IRIS}}$  as

$$w_{\text{bulk}}^{\text{IRIS}} = 1.2 \cdot n_e \cdot m_p \cdot \frac{v_{\text{bulk}}^2}{2} [\text{erg cm}^{-3}], \tag{5}$$

where  $n_e$  is the electron density, the factor 1.2 appears because of ions, and  $m_p$  is the proton mass (1.67  $\times$  10<sup>-24</sup> g). We use the electron density determined from the O IV line ratios and the Si IV Doppler velocities because of the better Gaussian fits due to the higher signal and because Si IV velocities were found to be very similar to the O IV velocities.

We determined which IRIS pixels lie inside the 50% RHESSI 6–9 keV contour and calculated the energy density for all of them (where possible, unless the densities were unavailable). We then obtained an average energy density inside this area (0.12 erg cm $^{-3}$ ) by averaging over the valid pixels. To estimate the total bulk kinetic energy within the flare footpoints  $W_{\rm bulk}^{\rm IRIS} = \int w_{\rm bulk}^{\rm IRIS} dV \sim w_{\rm bulk}^{\rm IRIS} V$ , we estimate the volume V as a product of the number of pixels (1711) inside the contour and the pixel volume, assuming a height of 1 Mm. IRIS observed with 0."166 pixel $^{-1} = 120$  km pixel $^{-1}$ , giving a pixel area of  $1.44 \times 10^{14}$  cm $^{2}$  and thus a volume of  $1.44 \times 10^{12}$  cm $^{3}$ . This gives a total bulk kinetic energy for this volume of  $W_{\rm bulk}^{\rm IRIS} \sim 3 \cdot 10^{24}$  erg.

# 6.4. Turbulent Kinetic Energy at the Flare Footpoints

We determined the turbulent kinetic energy density  $w_{\rm turb}^{\rm IRIS}$  similarly to  $w_{\rm bulk}^{\rm IRIS}$  in Section 6.3 by replacing  $v_{\rm bulk}$  with  $v_{\rm turb}$  in Equation (5) and considering the same valid pixels inside the 50% RHESSI contour. The average turbulent energy density in this area is 2.7 erg cm<sup>-3</sup>. Similarly to Section 6.3, we obtain the total energy by multiplying this energy density by the same volume as in Section 6.3. The total turbulent kinetic energy for this volume is then  $W_{\rm turb}^{\rm IRIS} \leq 7 \cdot 10^{25}$  erg, which is less than 0.1% of the flare thermal energy and about 0.15% of the nonthermal energy deposition. Neither  $W_{\rm bulk}^{\rm IRIS}$  nor  $W_{\rm turb}^{\rm IRIS}$  is shown in Figure 16, as they are indistinguishable from the bottom axis.

We compare this turbulent energy detected in the flare footpoints with the turbulent energy in a coronal flare volume. Kontar et al. (2017) employed the Hinode/EIS data to find the turbulent flare energy in a cusp region, which appeared to be less than 1% of the released energy at any given time instance. The kinetic turbulent energy at the flare footpoints detected here, presumably driven by precipitating particles, is one order of magnitude lower than that in the corona reported by Kontar et al. (2017).

# 6.5. Quantification of the Nonthermal Energy with X-Ray and Microwave Data and 3D Modeling

As previously mentioned, RHESSI missed the impulsive phase of the flare, while Konus-Wind recorded the impulsive phase in the G1 channel only in the waiting mode. Thus, nonthermal energy and the rate of the nonthermal energy deposition can only be estimated indirectly using the microwave spectrum and available microwave and Konus-Wind light curves. In Section 5.3 we determined the population of nonthermal electrons needed to reproduce the observed peak microwave spectrum that occurred at 06:44:41 UT.

The corresponding instant nonthermal energy is  $W_{nth} = 5.87 \times 10^{27}$  erg at that time.

Now, to estimate the nonthermal energy deposition rate, we need to estimate the escape time  $\tau_{\rm esc}$  of the nonthermal electrons from Loop II. To do so, we consider lag-correlation between the HXR G1 Konus-Wind light curve and the microwave light curves at 3.75 and 9.4 GHz obtained with NoRP. This lag-correlation analysis shows that the 9.4 GHz light curve is delayed by  $\sim$ 0.5 s relative to the Konus-Wind light curve, while the 3.75 GHz one is delayed by  $\sim$ 2 s. Thus, for our order-of-magnitude estimate, we select a characteristic value  $\tau_{\rm esc}=1$  s, which yields  $\dot{W}_{nth}\approx 5.87\times 10^{27}$  erg s<sup>-1</sup> at the flare peak time. To obtain the total deposition of the nonthermal energy, we multiply this peak value by the HXR light-curve duration, 8 s, at the level of half-maximum:  $W_{nth \text{ tot}}\approx 4.7\times 10^{28}$  erg.

The nonthermal energy  $W_{\text{nonth}}^{\text{RHESSI}}$  potentially captured by RHESSI after the impulsive phase was computed as a cumulative sum using the parameters from the RHESSI fits:

$$W_{\text{nonth}}^{\text{RHESSI}} = \int_{t_0}^{t} F_0 E_c \frac{\delta - 1}{\delta - 2} dt \text{ [erg]}, \tag{6}$$

where  $t_0$  is the end of the RHESSI night, while the  $F_0$ ,  $E_c$ , and  $\delta$  are the thick-target parameters (see Section 3.1) from the fitting of the RHESSI data displayed in Figures 6(c)–(e);  $W_{\rm nonth}^{\rm RHESSI}$  is shown in dashed blue in Figure 16. We note that these thick-target fit parameters, especially  $F_0$ , come with very large uncertainties and might overestimate the nonthermal energy deposition. However, as has been shown, the presence of such a nonthermal population does not contradict any available data. For example, the microwave emission produced by such a population does not overestimate the observed microwave emission. The presence of this nonthermal component is also consistent with the behavior of the thermal energy at the hot loop, which reaches the peak exactly when this nonthermal component is over.

# 6.6. Evolution of the Energy Partitions

Here we briefly summarize the evolution of the energy partitions at the course of the three phases of the flare: the preimpulsive, the impulsive, and the main phase. We only consider Loops I and II, as we do not have enough constraints to quantify evolution of Loop III. At the pre-impulsive phase, we observe a modest heating of Loops I ( $T \sim 9-10\,\mathrm{MK}$ ) and II ( $T \sim 13-14\,\mathrm{MK}$ ). No signature of any nonthermal component is present at this phase. This phase is followed by a very short (20 s) impulsive phase, when the release of the nonthermal energy observed in the microwave and HXR ranges is immediately followed by a thermal response in Loops I and II. The heating continues for a few more minutes into the main phase of the flare. Both pre-impulsive and main flare phases require an extra heating in addition to the heating due to nonthermal electron loss.

# 6.7. Magnetic Energy Available for the Flare

The above-described components of the flare energy must have come from the free magnetic energy available in the AR (Fleishman et al. 2020). To check whether the needed magnetic energy existed in the AR before the flare and to nail down its changes associated with the flare, we resort to 3D magnetic

reconstructions. To do so we fixed the Carrington coordinates of our model FOV and created sequences of potential and NLFFF reconstructions computed for seven consecutive time frames between 6:00 and 7:12 UT roughly centered at the flare time. This approach preserves the reconstruction volume for different time frames and minimizes possible uncertainties due to solar rotation. We employed two different disambiguation algorithms for the transverse component of the photospheric magnetic field (Metcalf 1994; Rudenko & Anfinogentov 2014) and found only very minor differences between solutions, which cross-validates them.

The total magnetic energy in each data cube is straightforwardly computed as  $W_B = \int B^2 dV/(8\pi)$ , which fluctuates less than 1% around  $\approx 1.2 \times 10^{33}$  erg for all our potential extrapolations and around  $\approx 1.1 \times 10^{33}$  erg for the NLFFF extrapolations. Therefore, we cannot derive the free magnetic energy because the magnetic energy in all NLFFF cubes appeared slightly smaller, by less than 10% in all cases, than the corresponding potential magnetic energy. This is a known problem of reconstruction algorithms associated with numerical residuals of  $\nabla \cdot \boldsymbol{B}$ , which are theoretically equivalent to zero, but not in the numerical solutions (De Rosa et al. 2015).

We estimated uncertainties of the total magnetic energy as follows: (i) by finding differences of the total magnetic energy between two successive (in time) data cubes and (ii) by finding differences between two simultaneous models extrapolated from the bottom boundary condition obtained with two different  $\pi$ -disambiguation methods (Metcalf 1994; Rudenko & Anfinogentov 2014). The magnetic energy uncertainties estimated this way are above  $\sim 3 \times 10^{30}$  erg. This is more than one order of magnitude above the required flare energy,  $\sim 10^{29}$  erg; thus, the decrease of the magnetic energy due to the flare cannot be detected using the NLFFF extrapolation method. The total energy released in the flare composes less than 0.01% of the total magnetic energy. We conclude that the presence of the required free magnetic energy in this AR is highly likely.

#### 7. Discussion

In this study, we have analyzed energy partitioning, its evolution, and spatial distribution in flaring loops. We found three distinct consecutive heating episodes, but only one episode of nonthermal emission. The first preheating episode (a precursor?) preceded the nonthermal impulsive peak, the second one appeared as a response on the impulsive peak, while the third one occurred later at the main flare phase without any obvious connection with the impulsive nonthermal peak. From the timing of the event, we can conclude that only a portion of the flaring plasma heating was driven by nonthermal electron losses, while the remaining portion was driven by another agent, which could be, e.g., a direct heating by magnetic reconnection, or heating by accelerated ions, or something else.

The distribution of the energy components over the three flaring loops involved in the event is highly uneven. While the plasma heating takes place in all three loops, the nonthermal electrons are present in one loop only—that showing the strongest plasma heating. The nonthermal energy deposition is sufficient for the post-impulsive heating in the flaring loop with nonthermal electrons, while it is insufficient for the first and third heating episodes.

The flare-integrated energies are (i) the thermal energy  $\sim 10^{29}$  erg, (ii) the nonthermal energy deposition  $\sim 5 \times 10^{28}$  erg,

(iii) the turbulent kinetic energy at the footpoints  $\sim 7 \times 10^{25}$  erg, and (iv) the bulk kinetic energy at the footpoints  $\sim 3 \times 10^{24}$  erg. These compose less than 0.01% of the total magnetic energy of the AR.

The kinetic energy detected in our study, presumably driven by nonthermal electrons precipitating at the footpoints, represents only a minor fraction of the released energy and so is energetically unimportant. We note that kinetic energy of plasma motions could be measured in UV, EUV, and soft X-rays and the different spectral lines tell us about moving plasma at different temperatures and in different layers of flaring atmosphere. So the kinetic energy (energy density) estimates could be different for different parts of a flare. With IRIS UV data we have only estimated a portion of the kinetic energies in the flare footpoint, while this energy remains unconstrained in the flare coronal volume. The only available coronal spectral line in our case is Fe XXI, sensitive to the 10 MK plasma, which is weak and not suitable for quantitative fitting with a Gaussian spectral profile. In principle, some portion of the kinetic energy in the corona could be estimated from apparent motions of the hot flaring plasma, which are, however, not seen in the animated Figure 7, where all apparent changes indicate a temporal evolution of the plasma temperature and EM, rather than any change of the source morphology, which could be attributed to plasma motions. This means that no available diagnostic reveals any measurable coronal kinetic energy in this flare.

The flare properties summarized above place our event somewhere in between "normal" flares with a thermal precursor and nonthermally dominated ("cold") flares. The estimated total deposition of the nonthermal energy is only a factor of two lower than the detected thermal energy; considering the uncertainties of these estimates, this might be sufficient to account for the thermal energy of the flare in agreement with the conclusion of Emslie et al. (2012) obtained for a set of powerful flares. However, the detailed analysis of timing of thermal and nonthermal emissions, as well as of spatial placements of the thermal and nonthermal energies between the three flaring magnetic flux tubes, rules out such an option. Meanwhile, one of the flaring loops, Loop II in our model, shows close similarity to the nonthermally dominated "cold" flares: there is a clear Neupert effect timing between the impulsive nonthermal emission and thermal response in Loop II, although even here a preheating is detected. The nonthermal energy deposition matches well the thermal energy detected in this flare, while the associated kinetic energy from the flare footpoints adds only a minor fraction to the overall energy budget. This implies that the nonthermal energy is primarily dissipated to the thermal energy rather than to bulk or random motions of the ambient plasma.

For comparison, in the nonthermally dominated 2013 November 05 flare described in Paper I, all (two) flaring loops contain accelerated nonthermal electrons and are heated owing only to losses of those nonthermal electrons. The nonthermal electrons were divided roughly equally between those loops, but the thermal responses of those loops were different from each other. Motorina et al. (2020) proposed that the thermal response of a loop differs depending on the initial plasma density in the loop just before the episode of the energy release. In the 2014 February 16 flare, studied here, we observe more dissimilarity between the loops involved in the flaring. Only one of them contains a detectable amount of nonthermal

electrons (at the peak time), and only in that loop where the heating is dominated by losses of the nonthermal electrons. Two other flaring loops are heated, presumably, by some other means. We note that the initial densities in the loops are different from each other. The nonthermal electrons are observed in the most tenuous and hottest of the three loops. This loop is heated up to highest temperatures compared with the "directly" heated loops. A similar behavior, with the largest temperature detected in the most tenuous loop, is detected in the nonthermally dominated 2013 November 05 flare. We therefore propose that not only the magnetic structure in the flaring volume but also the initial distribution of the thermal plasma play a crucial role in deciding how the released energy is apportioned between the thermal and nonthermal components and how these energies are divided between various flaring loops.

This work was partly supported by NSF grants AGS-1817277 and AGS-1743321 and NASA grants 80NSSC18K0667, 80NSSC19K0068, 80NSSC18K1128, and 80NSSC20K0627 to the New Jersey Institute of Technology. G.M. (SDO/AIA and RHESSI data analysis) acknowledges support from RSF grant 20-72-10158. E.P.K. was supported by STFC consolidated grant ST/P000533/1. We are thankful to Alexandra Lysenko for fruitful discussions of the Konus-Wind data.

#### **ORCID iDs**

```
Gregory D. Fleishman https://orcid.org/0000-0001-5557-2100
Lucia Kleint https://orcid.org/0000-0002-7791-3241
Galina G. Motorina https://orcid.org/0000-0001-7856-084X
Gelu M. Nita https://orcid.org/0000-0003-2846-2453
Eduard P. Kontar https://orcid.org/0000-0002-8078-0902
```

#### References

```
Anfinogentov, S. A., Stupishin, A. G., Mysh'yakov, I. I., & Fleishman, G. D.
   2019, ApJL, 880, L29
Aptekar, R. L., Frederiks, D. D., Golenetskii, S. V., et al. 1995, SSRv, 71, 265
De Pontieu, B., Title, A. M., Lemen, J. R., et al. 2014, SoPh, 289, 2733
De Rosa, M. L., Wheatland, M. S., Leka, K. D., et al. 2015, ApJ, 811, 107
Doschek, G. A., Warren, H. P., & Young, P. R. 2016, ApJ, 832, 77
Emslie, A. G., Dennis, B. R., Shih, A. Y., et al. 2012, ApJ, 759, 71
Fleishman, G., Mysh'yakov, I., Stupishin, A., Loukitcheva, M., &
   Anfinogentov, S. 2019, ApJ, 870, 101
Fleishman, G. D., Anfinogentov, S., Loukitcheva, M., Mysh'yakov, I., &
  Stupishin, A. 2017a, ApJ, 839, 30
Fleishman, G. D., Gary, D. E., Chen, B., et al. 2020, Sci, 367, 278
Fleishman, G. D., Nita, G. M., & Gary, D. E. 2017b, ApJ, 845, 135
Fleishman, G. D., Pal'shin, V. D., Meshalkina, N., et al. 2016, ApJ, 822, 71
Flower, D. R., & Nussbaumer, H. 1975, A&A, 45, 145
Golub, L., Deluca, E., Austin, G., et al. 2007, SoPh, 243, 63
Grechnev, V. V., Lesovoi, S. V., Smolkov, G. Y., et al. 2003, SoPh, 216, 239
Guidice, D. A., Cliver, E. W., Barron, W. R., & Kahler, S. 1981, BAAS,
   13, 553
Hannah, I. G., & Kontar, E. P. 2012, A&A, 539, A146
Hannah, I. G., & Kontar, E. P. 2013, A&A, 553, A10
Hurford, G. J., Schmahl, E. J., Schwartz, R. A., et al. 2002, SoPh, 210, 61
Jeffrey, N. L. S., Fletcher, L., & Labrosse, N. 2016, A&A, 590, A99
Kontar, E. P., Jeffrey, N. L. S., & Emslie, A. G. 2019, ApJ, 871, 225
Kontar, E. P., Perez, J. E., Harra, L. K., et al. 2017, PhRvL, 118, 155101
Kosugi, T., Matsuzaki, K., Sakao, T., et al. 2007, SoPh, 243, 3
Kuroda, N., Gary, D. E., Wang, H., et al. 2018, ApJ, 852, 32
Lemen, J. R., Title, A. M., Akin, D. J., et al. 2012, SoPh, 275, 17
Lin, R. P., Dennis, B. R., Hurford, G. J., et al. 2002, SoPh, 210, 3
Lysenko, A. L., Altyntsev, A. T., Meshalkina, N. S., Zhdanov, D., &
   Fleishman, G. D. 2018, ApJ, 856, 111
```

Metcalf, T. R. 1994, SoPh, 155, 235
Motorina, G. G., Fleishman, G. D., & Kontar, E. P. 2020, ApJ, 890, 75
Muratov, A. A. 2011, in XIIth Conf. Young Scientists 365, Baikal Young Scientists' Int. School (Irkutsk: Institute of Solar-Terrestrial Physics), 85
Nakajima, H., Nishio, M., Enome, S., et al. 1994, IEEEP, 82, 705
Neupert, W. M. 1968, ApJL, 153, L59
Nita, G. M., Fleishman, G. D., Kuznetsov, A. A., Kontar, E. P., & Gary, D. E. 2015, ApJ, 799, 236
Nita, G. M., Viall, N. M., Klimchuk, J. A., et al. 2018, ApJ, 853, 66

Pal'shin, V. D., Charikov, Y. E., Aptekar, R. L., et al. 2014, Ge&Ae, 54, 943

Polito, V., Del Zanna, G., Dudík, J., et al. 2016, A&A, 594, A64 Rudenko, G. V., & Anfinogentov, S. A. 2014, SoPh, 289, 1499 Scherrer, P. H., Schou, J., Bush, R. I., et al. 2012, SoPh, 275, 207 Tian, H., DeLuca, E. E., Cranmer, S. R., et al. 2014, Sci, 346, 1255711 Tikhonov, A. N. 1963, Soviet Math. Dokl., 4, 1035 Torii, C., Tsukiji, Y., Kobayashi, S., et al. 1979, PRIAN, 26, 129 Warren, H. P., Brooks, D. H., Ugarte-Urra, I., et al. 2018, ApJ, 854, 122 White, S. M., Thomas, R. J., & Schwartz, R. A. 2005, SoPh, 227, 231 Young, P. R., Keenan, F. P., Milligan, R. O., & Peter, H. 2018, ApJ, 857, 5 Zhdanov, D. A., & Zandanov, V. G. 2015, SoPh, 290, 287